PAPER

Check for updates

Electrostatically confined Bi/Ti$_3$C$_2$T$_x$ on a sponge as an easily recyclable and durable catalyst for the reductive transformation of nitroarenes†

Changqiang Yu,[a] Linfen Peng,[a] Yisong Zhu,[a] Guanshun Xie,[a] Zhenjun Wu,[b] Xiuqiang Xie [ID] *[a] and Nan Zhang [ID] *[a]

Developing novel catalysts with both easily accessible recyclability and long-term durability toward chemical synthesis is highly desirable yet remains to be explored. In this work, a porous and bulk sponge-confined bismuth (Bi)/Ti$_3$C$_2$T$_x$ (MXene) composite as a monolithic catalyst is synthesized *via* the photodeposition of Bi nanoparticles with a mean size of 4.4 nm on Ti$_3$C$_2$T$_x$ followed by electrostatic self-assembly between the negatively charged Bi/Ti$_3$C$_2$T$_x$ and positively charged sponge. It is noteworthy that compared to the analogue of widely investigated reduced graphene oxide, Ti$_3$C$_2$T$_x$ with favorable hydrophilic surface groups as the scaffold for the high dispersion of Bi nanoparticles benefits not only efficient aqueous phase catalytic reactions, but also strong electrostatic interaction with the sponge substrate for ensuring the recyclability towards practical applications. As a result, the bulk sponge-confined Bi/Ti$_3$C$_2$T$_x$ as an easily recyclable catalyst possesses both improved catalytic performance and long-term durability for the hydrogenation of nitroarenes in the aqueous phase. This study presents a facile and valuable protocol for functionalizing inexpensively available porous bulk materials to confine catalysts towards integrated materials featuring easy-separation and long-term stability for practical catalytic processes.

1 Introduction

Catalytic hydrogenation using sodium borohydride (NaBH$_4$) as a reductant represents an advanced and promising process for simultaneously detoxicating and reducing nitroarenes into amines.[1–5] Catalysts are indispensable for capably catalyzing NaBH$_4$ to afford this process.[6,7] Among the reported catalysts, Au,[8] Ag,[6] Cu,[9] Pd,[5] Pt,[10] and metal alloys[11–16] have been proved to be thermodynamically favorable, considerably efficient, and catalytically durable for NaBH$_4$-participating nitroarene hydrogenation reactions.[1,17–19] Especially, nanometal bismuth (Bi) has practical potential for catalyzing nitroarene hydrogenation with the consideration of both the merits mentioned above and the low cost.[20,21] However, the agglomeration of nanometals into bulk ones resulting from high surface free energy leads to poor catalytic efficiency.[22,23] It has been demonstrated that the introduction of supporting materials can not only act as a crystal-growth mediator by providing nucleation and growth sites, but also alleviate the agglomeration of nanometals to

unveil abundant active sites for enhancing catalytic reactivity.[15,24–26] Furthermore, supporting materials can also stabilize nanomaterials through interfacial interaction.[27]

Graphene oxide (GO) is a widely used surface functional group-terminated two-dimensional (2D) material with a large surface area and is proved to be promising for assembling nanomaterials.[28,29] However, GO is inevitably converted into reduced graphene oxide (rGO) during the anchoring of metal nanoparticles, which therefore ruins surface properties.[30,31] MXenes represent 2D metal carbides, nitrides, and carbonitrides with the formula of M$_{n+1}$X$_n$T$_x$, where $n = 1$, 2, 3, and 4, M represents transition metals, X corresponds to carbon and/or nitrogen, and T$_x$ stands for terminal groups.[32–35] The large surface area, rich surface groups, and opportune stability towards redox surroundings make 2D MXenes competent for assembling nanometals to achieve reinforced aqueous catalytic activity.[36–39] Hitherto, the anchoring of Bi nanoparticles on MXenes for catalyzing NaBH$_4$ to hydrogenate nitroarenes remains to be explored. Thus, it is of significance to devote efforts towards examining the catalytic hydrogenation activity of Bi/MXene composites towards the reduction of nitroarenes.

The use of integrated catalysts avoids the time-consuming and complicated separation of powder catalysts from catalytic systems, which simplifies the catalytic process, saves energy, and elevates efficiency.[40,41] Additionally, the loss of powder catalysts during the recycling process accounts for the poor

[a]College of Materials Science and Engineering, Hunan University, Changsha 410082, China. E-mail: nanzhang@hnu.edu.cn; xiuqiang_xie@hnu.edu.cn

[b]College of Chemistry and Chemical Engineering, Hunan University, Changsha 410082, China

† Electronic supplementary information (ESI) available. See DOI: 10.1039/d1ta02736k

This journal is © The Royal Society of Chemistry 2021

J. Mater. Chem. A, 2021, **9**, 19847–19853 | **19847**

cyclability of nanometals to a large extent. In this context, an integrated catalyst is of great value in practical catalytic chemical synthesis. Enlighted by the superior cyclability of catalysts assembled on porous materials,[42–44] and the electrostatically strong interaction between $Ti_3C_2T_x$ and catalysts, which imparts $Ti_3C_2T_x$/semiconductor hybrids with unique durability,[32] in this work, we evenly assemble Bi nanoparticles on a $Ti_3C_2T_x$ platform with small size, abundant catalytically active sites, and strong interfacial chemical interaction *via* a facile photodeposition process. The as-synthesized $Bi/Ti_3C_2T_x$ catalyst shows enhanced activity and durability for hydrogenating a class of nitroarenes. Electrostatically confined $Bi/Ti_3C_2T_x$ onto a bulk sponge enables easy recyclability without compromising durability.

2 Experimental section

2.1. Synthesis of $Ti_3C_2T_x$ MXene nanoflakes

$Ti_3C_2T_x$ nanoflakes are obtained *via* selectively etching the Ti_3AlC_2 precursor with a mixture of hydrochloric acid and lithium fluoride. Firstly, 20.0 mL hydrochloric acid (9 M) and 1.6 g lithium fluoride are mixed and magnetically stirred for 10 min. Then, 1.0 g Ti_3AlC_2 is introduced into the mixture and held at 40 °C for 24 h. Deionized water is used to wash the final product to ensure that the pH of supernatant is around 6.0. Subsequently, the final precipitate is diluted with 100.0 mL deionized water, sonicated under a nitrogen atmosphere for 1.5 h at 25 °C, and centrifuged at a speed of 3500 rpm for 1.5 h to acquire the $Ti_3C_2T_x$ colloid. Finally, the concentration of $Ti_3C_2T_x$ nanoflakes is determined by filtering and drying 4.0 mL of the colloid in a vacuum. The $Ti_3C_2T_x$ colloid with desired concentration (2.0 mg mL^{-1}) is obtained by diluting the known-concentration $Ti_3C_2T_x$ colloid with deionized water.

2.2. Synthesis of $Bi/Ti_3C_2T_x$

$Bi/Ti_3C_2T_x$ is fabricated through a facile photodeposition method (Fig. 1a). In detail, 30.0 mL deionized water is mixed with 10.0 mL lactic acid, 1.0 g polyethylene glycol, and 0.3 g bismuth ammonium citrate to form translucent solution. Then, different volumes (250 μL, 500 μL, and 750 μL) of $Ti_3C_2T_x$ colloid (2.0 mg mL^{-1}) are added, stirred for 30 min, sealed in a photoreactor, bubbled with nitrogen to remove air, and illuminated with a 200 W Xe lamp (PLS-SXE300D, Beijing Perfectlight) for 4 h. Temperature-controlled cycling water is used to make sure that the temperature of reaction system is 25 °C, and nitrogen is continuously bubbled during the whole experiment. The final product is rinsed sequentially with ethanol and deionized water, freezingly dried, and labelled Bi–0.5% $Ti_3C_2T_x$, Bi–1.0% $Ti_3C_2T_x$, and Bi–1.5% $Ti_3C_2T_x$. GO is also used to synthesize a Bi–rGO composite in the same way as $Ti_3C_2T_x$. For comparison, pure Bi is also synthesized in the same way except for the absence of $Ti_3C_2T_x$.

2.3. Synthesis of the APTES-modified sponge

The porous bulk sponge (2.0 cm in width, 2.0 cm in height, and 0.3 cm in thickness) is immersed in a solution containing 0.4 mL APTES and 50.0 mL anhydrous ethanol. The system is then maintained at 60 °C for 4 h. The modified porous bulk sponge is washed with ethanol and deionized water to dislodge surplus APTES.

2.4. Synthesis of sponge-confined $Bi/Ti_3C_2T_x$

An electrostatic self-assembly process is carried out to synthesize the sponge-confined $Bi/Ti_3C_2T_x$ or Bi/rGO (Fig. 1a). Typically, the APTES-modified porous bulk sponge is immersed in a suspension composed of 60.0 mL deionized water and 2.0 mg $Bi/Ti_3C_2T_x$ or Bi/rGO composites, followed by magnetic stirring. Afterwards, the sponge with $Bi/Ti_3C_2T_x$ or Bi/rGO composites electrostatically confined onto its skeleton is dried at 60 °C for 4 h in a vacuum.
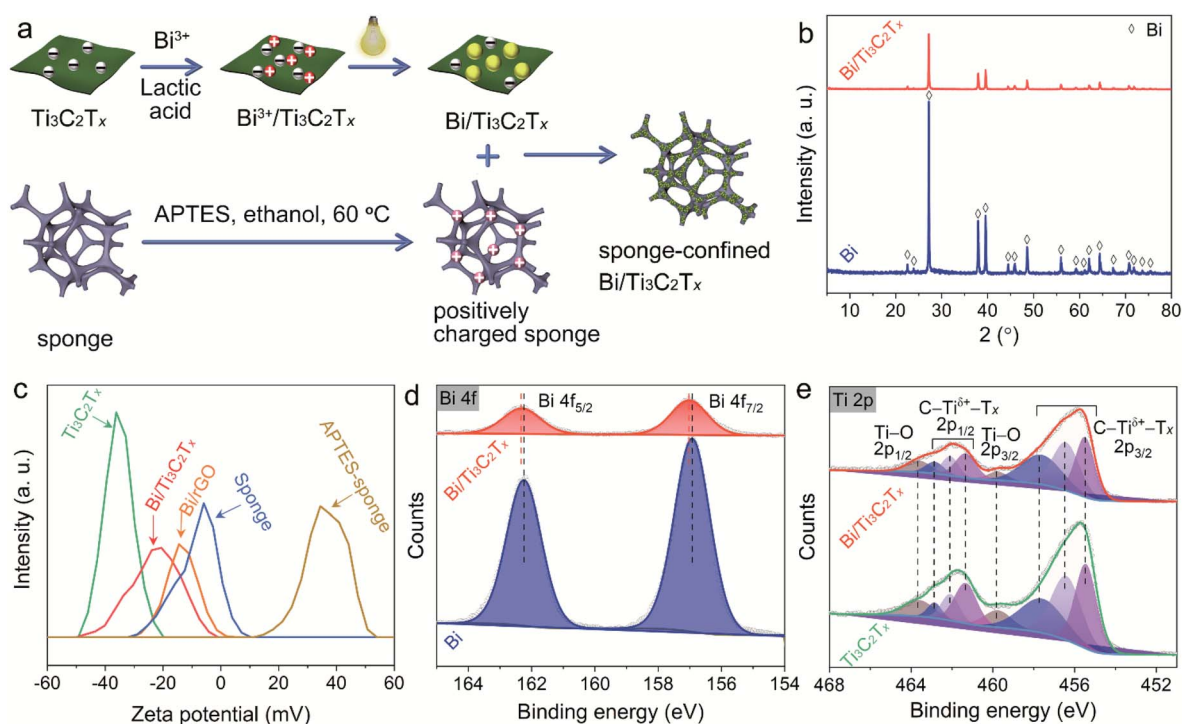
2.5. Characterization

The phase composition is verified by X-ray diffraction (XRD) with a miniFlex diffractometer (Rigaku, Japan). Raman spectra are obtained by using an inVia-reflex spectrometer (Renishaw, UK). Surface charge properties are detected with a Zetasizer Nano ZSP instrument (Malvern, UK). X-ray photoelectron spectra (XPS) signals are gathered by using a K-ALPHA apparatus (Thermo Fisher Scientific, USA). The morphology is analyzed with a S-4800 scanning electron microscope (SEM, Hitachi, Japan). The microstructure is analyzed *via* a Titan G2 60-300 transmission electron microscope (TEM, FEI, USA). The contacting angle is tested by using a DSA100 machine (Kruss, Germany). Ultraviolet-visible (UV-vis) adsorption spectra are record using an UV-1780 spectrophotometer (Shimadzu, Japan). An ASAP 2020 instrument (Micromeritics, USA) is employed to investigate surface properties.

2.6. Catalytic activity

The hydrogenation of nitroarenes with $NaBH_4$ as the reductant is performed to test the catalytic activity of the as-synthesized $Bi/Ti_3C_2T_x$ and sponge-confined $Bi/Ti_3C_2T_x$. In detail, 10.0 mL $Bi/Ti_3C_2T_x$ suspension with a concentration of 0.1 mg mL^{-1} is mixed with 40.0 mL of 10.0 mg L^{-1} 4-NA under magnetic stirring for 30 min. Afterwards, 10.0 mL of 0.1 M $NaBH_4$ is introduced to initiate catalytic reduction reactions. A suspension with a volume of 2.0 mL is collected at a given time interval by using a syringe and filtered by passing through a 0.22 μm polyethersulfone film to obtain the solution for measuring optical absorbance at the maximum absorption wavelength using a UV-vis spectrophotometer. For sponge-confined $Bi/Ti_3C_2T_x$, it is immersed in 60.0 mL 4-NA solution, and the dosage of $NaBH_4$ is 15.0 mL (Fig. S1†). The reused sponge-confined $Bi/Ti_3C_2T_x$ is immersed in ethanol and deionized water to achieve recovery.

3 Results and discussion

As can be seen from Fig. S2,† the diffraction peaks at 9.45°, 18.89°, 33.60°, 36.5°, 38.48°, 41.22°, 47.91°, 51.90°, 55.81°, 59.62°, 64.81°, 69.59°, 73.20°, and 74.63° correspond to the (002), (004), (101), (103), (104), (105), (107), (108), (109), (110), (1,0,11), (1,0,12), (118), and (204) planes of hexagonal Ti_3AlC_2

19848 | *J. Mater. Chem. A*, 2021, **9**, 19847–19853

This journal is © The Royal Society of Chemistry 2021

Fig. 1 (a) Schematics of the synthesis of Bi/$Ti_3C_2T_x$ and sponge-confined Bi/$Ti_3C_2T_x$. (b) XRD patterns of Bi and Bi/$Ti_3C_2T_x$. (c) Zeta potentials of $Ti_3C_2T_x$, Bi/$Ti_3C_2T_x$, Bi/rGO, sponge, and APTES-modified sponge. (d) High-resolution Bi 4f XPS spectra of Bi and Bi/$Ti_3C_2T_x$. (e) High-resolution Ti 2p XPS spectra of $Ti_3C_2T_x$ and Bi/$Ti_3C_2T_x$.

(JCPDS 52-0875), respectively. The peak of Ti_3AlC_2 (002) shifts from 9.45° to 7.22° with selective etching of Al, revealing the formation of a $Ti_3C_2T_x$ MXene.[45] For bare Bi, the peaks that appeared at 22.46°, 23.74°, 27.15°, 37.40°, 39.61°, 44.55°, 45.91°, 48.71°, 56.05°, 59.33°, 61.12°, 62.17°, 64.51°, 67.46°, 70.80°, 71.88°, 72.91°, and 74.58° correspond to the (003), (101), (012), (104), (110), (015), (006), (202), (024), (107), (205), (116), (122), (018), (214), (300), (027), and (125) planes of rhombohedral Bi metal (JCPDS 05-0519) (Fig. 1b). The diffraction peaks of Bi metal are clearly detected with the introduction of $Ti_3C_2T_x$, proving the coexistence of Bi and $Ti_3C_2T_x$. No additional diffraction peaks appear in the patterns of the samples. The Raman spectrum of Bi/$Ti_3C_2T_x$ is identical to that of $Ti_3C_2T_x$, which indicates that $Ti_3C_2T_x$ is stable during the photodeposition of Bi nanoparticles (Fig. S3†).

According to Fig. 1c, the zeta potential of pristine $Ti_3C_2T_x$ is −36.1 mV, which enables the electrostatic absorption of Bi^{3+} onto $Ti_3C_2T_x$ to afford *in situ* growth of Bi nanoparticles. The zeta potential of Bi/$Ti_3C_2T_x$ is −20.7 mV, which is less negative than that of pristine $Ti_3C_2T_x$. This can be ascribed to the partial shielding of Bi towards the functional groups of $Ti_3C_2T_x$. The sponge is successfully modified with APTES with its zeta potential changing from −5.9 mV to +34.6 mV to enable the electrostatic self-assembly process. As a result, Bi/$Ti_3C_2T_x$ can be electrostatically confined onto the porous bulk sponge.

High-resolution Bi 4f XPS shows two peaks at 162.24 eV (Bi $4f_{5/2}$) and 156.91 eV (Bi $4f_{7/2}$) (Fig. 1d), confirming the successful anchoring of Bi on $Ti_3C_2T_x$ through a facile photodeposition process.[46] The Bi 4f XPS spectra of Bi/$Ti_3C_2T_x$ shift to higher

binding energies, which implies that Bi has chemically bonded with $Ti_3C_2T_x$. High-resolution Ti 2p XPS spectra can be fitted into eight peaks according to the valence state of Ti ions in $Ti_3C_2T_x$ (Fig. 1e). The Ti $2p_{1/2}$ (462.88 eV, 462.10 eV, and 461.33 eV) and Ti $2p_{3/2}$ (457.72 eV, 456.47 eV, and 452.51 eV) XPS spectra are assigned to C–$Ti^{\delta+}$–T_x (δ = 1, 2, and 3).[47] Two other peaks of 463.66 eV ($2p_{1/2}$) and 459.82 eV ($2p_{3/2}$) are mainly caused by the Ti–O group.[48] Correspondingly, the contents of Ti–O bonds for $Ti_3C_2T_x$ and Bi/$Ti_3C_2T_x$ obtained from XPS analysis are 11.85% and 12.22%, respectively. The almost unchanged content of Ti–O bonds in Bi/$Ti_3C_2T_x$ further confirms the stability of $Ti_3C_2T_x$ during the photodeposition of Bi. The C 1s XPS spectra of $Ti_3C_2T_x$ have four peaks at 288.40 eV, 286.30 eV, 284.71 eV, and 281.45 eV (Fig. S4†), reflecting the existence of C–F, C–O, C–C, and C–Ti bonds in $Ti_3C_2T_x$.[49]

$Ti_3C_2T_x$ nanoflakes are confirmed by both SEM and TEM with a size of 50–200 μm (Fig. S5a and b†). Pure Bi particles with a size of 200–800 nm are well crystalized as their crystal faces are clearly exposed (Fig. 2a). It is difficult to observe metallic Bi on $Ti_3C_2T_x$ (Fig. 2b) due to small particle sizes that are beyond the resolution of SEM. Energy dispersive X-ray (EDX) spectra authenticate the presence of Ti, C, O, Bi, F, and Cl elements in Bi/$Ti_3C_2T_x$ (Fig. 2b, inset). The porous bulk sponge with a smooth surface is observed (Fig. S5c†), which contributes to absorbing and supporting catalysts. From Fig. 2c, it can be seen that Bi/$Ti_3C_2T_x$ is fully assembled on the sponge skeleton, verifying the successful synthesis of sponge-confined Bi/$Ti_3C_2T_x$ *via* the electrostatic self-assembly process. The shape of sponge-confined Bi/$Ti_3C_2T_x$ is well preserved (Fig. 2d), which is
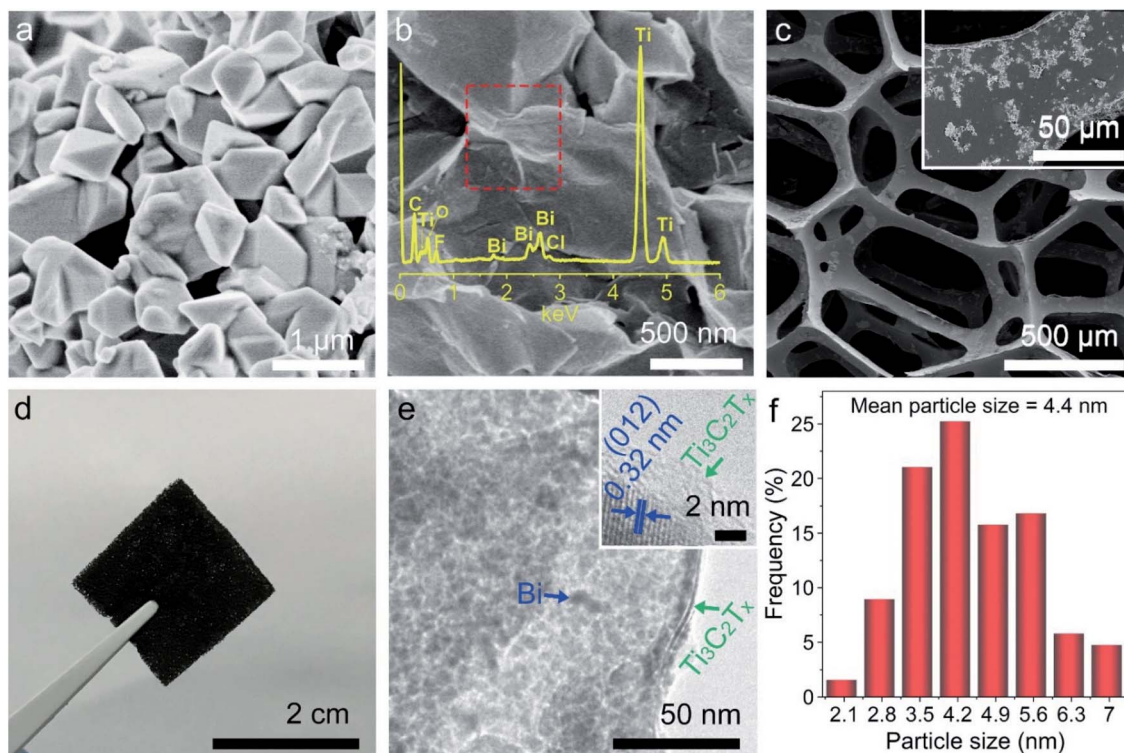
This journal is © The Royal Society of Chemistry 2021

J. Mater. Chem. A, 2021, **9**, 19847–19853 | **19849**

Fig. 2 SEM images of (a) Bi and (b) Bi/$Ti_3C_2T_x$ (inset is EDX spectra). (c) SEM and (d) photograph of sponge-confined Bi/$Ti_3C_2T_x$. (e) TEM images of Bi/$Ti_3C_2T_x$ (inset shows the high-resolution image). (f) Particle size distribution of Bi nanoparticles anchored on $Ti_3C_2T_x$.

conductive to practical applications. TEM is further utilized to explore the morphology and microstructure of the samples. As evidently shown in Fig. 2e, Bi nanoparticles are fully anchored on $Ti_3C_2T_x$ with a mean particle size of 4.4 nm (Fig. 2f), which means that Bi nanoparticles possess high surface energy and can interact with $Ti_3C_2T_x$ by virtue of their large surface area. The distance of 0.32 nm between two lattice fringes (Fig. 2e and S5d,† insets) matches well with the d value of the Bi (012) plane, which is consistent with phase composition analysis on the basis of XRD.

The catalytic ability of the as-fabricated Bi/$Ti_3C_2T_x$ powder catalysts is assessed by catalyzing $NaBH_4$ to transform 4-nitroaniline (4-NA) into p-phenylenediamine (PPD) (Fig. S6†). Fig. 3a shows the catalytic activities of 4-NA under various systems. The

adsorption capacities of $Ti_3C_2T_x$, Bi, and Bi/$Ti_3C_2T_x$ for 4-NA are 7.21%, 8.06%, and 11.38%, respectively. $NaBH_4$ alone does not hydrogenate 4-NA, revealing the essential role of the catalyst. This is because the reduction of nitroarenes with $NaBH_4$ is kinetically impeded by the high activation barrier.[50] Apparently, 4-NA is completely reduced to PPD by $NaBH_4$ within 6 min over Bi–1.0% $Ti_3C_2T_x$, while the conversion rate reaches only 58.21% for pristine metallic Bi. Thus, the role of $Ti_3C_2T_x$ in strengthening the conversion of Bi towards reducing 4-NA is confirmed, which generally comes from the high surface-to-volume ratio of $Ti_3C_2T_x$ supported Bi nanoparticles.

The effect of the contents of $Ti_3C_2T_x$ in Bi/$Ti_3C_2T_x$ on catalytic activity is also investigated (Fig. 3b). The optimum weight ratio of $Ti_3C_2T_x$ to Bi is 1.0% and both decreasing and
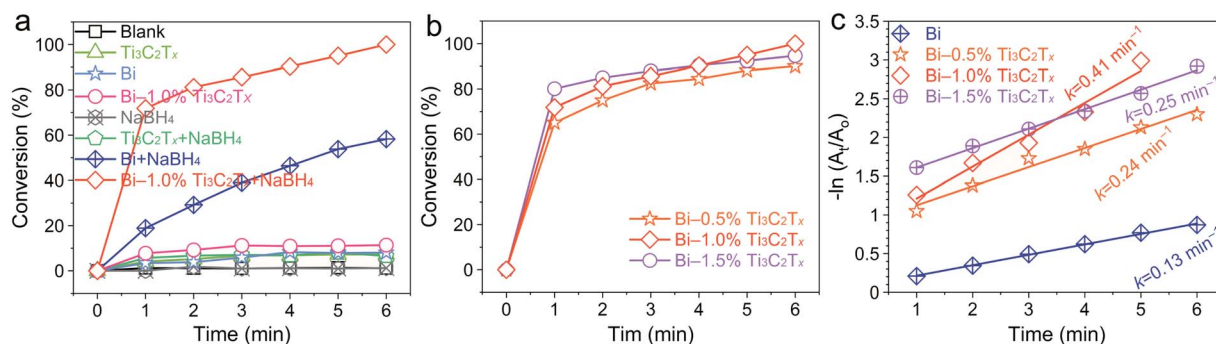

Fig. 3 (a) Catalytic hydrogenation of 4-NA in various systems. The effect of $Ti_3C_2T_x$ content in Bi/$Ti_3C_2T_x$ on the catalytic activity (b) and corresponding pseudo-first-order kinetic plots (c).
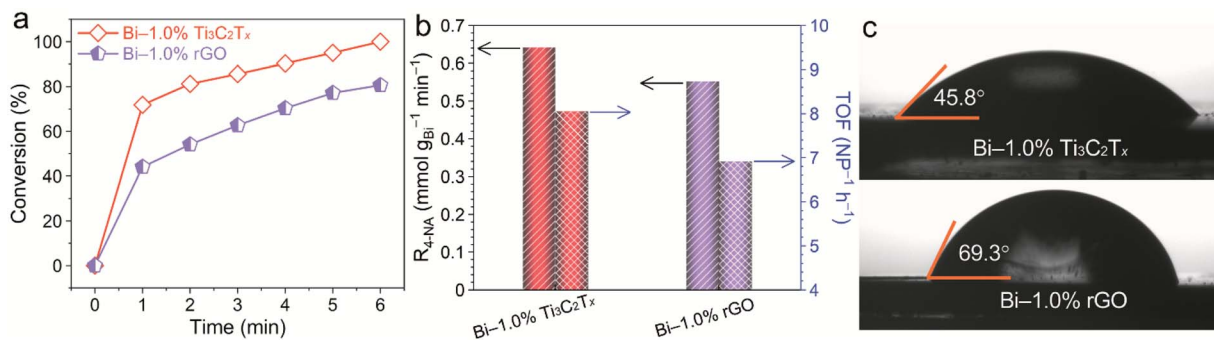
Fig. 4 (a) The time on-line conversion curves of 4-NA and (b) 4-NA conversion rates and TOF over Bi–1.0% $Ti_3C_2T_x$ and Bi–1.0% rGO powders. (c) Contact angles of Bi–1.0% $Ti_3C_2T_x$ and Bi–1.0% rGO with water.

increasing the weight ratio of $Ti_3C_2T_x$ lead to the deterioration of catalytic activity. The reason may be that a lower $Ti_3C_2T_x$ loading (0.5%) is unable to disperse metallic Bi well to efficiently expose active sites, while a high $Ti_3C_2T_x$ loading amount (1.5%) hinders metallic Bi nanoparticles from catalyzing $NaBH_4$. According to the fitted pseudo-first-order kinetic plots for Bi/$Ti_3C_2T_x$ with vary loading amounts of $Ti_3C_2T_x$ (Fig. 3c), Bi–1.0% $Ti_3C_2T_x$ possesses the largest apparent reaction rate constant of 0.41 min^{-1}, which is three times larger than that of pristine Bi and is comparable to that of noble metal-based catalysts (Table S1†). Additionally, Bi–1.0% $Ti_3C_2T_x$ also shows enhanced catalytic activity for the hydrogenation of 3-nitroaniline (3-NA), 2-nitroaniline (2-NA), 4-nitroanisole, and 4-nitrotoluene (Fig. S7†).

For comparison, Bi/rGO counterparts have been prepared in a similar process. XPS (Fig. S8†) and SEM (Fig. S9†) confirm the successful growth of metallic Bi onto GO and the electrostatic self-assembly between Bi–1.0% rGO and the APTES-modified sponge, respectively. The conversion (%) of 4-NA within 6 min over Bi–1.0% rGO powder is 80.6%, which is smaller than that of Bi–1.0% $Ti_3C_2T_x$ (99.5%) (Fig. 4a). Additionally, as shown in Fig. S10,† the adsorption ability of Bi–1.0% $Ti_3C_2T_x$ for 4-NA (11.3%) is higher than that of Bi–1.0% rGO (5.9%). We further employ characterization technologies to gain insight into the factors that differentiate catalytic activity between the two catalysts. Based on nitrogen adsorption–desorption analysis (Fig. S11†), the specific surface area and total pore volume of Bi–

1.0% rGO (100.5 m^2 g^{-1} and 0.05 cm^3 g^{-1}) are larger than those of Bi–1.0% $Ti_3C_2T_x$ (64.2 m^2 g^{-1} and 0.04 cm^3 g^{-1}) and Bi (5.5 m^2 g^{-1} and 0.03 cm^3 g^{-1}) (Table S2†). Besides, the mean particle size of Bi nanoparticles in Bi–1.0% rGO is 1.46 nm (Fig. S12†), which is smaller than that of Bi–1.0% $Ti_3C_2T_x$ (4.4 nm). Theoretically, the fully dispersed Bi nanoparticles on rGO with abundant active sites ought to be more catalytically active. The conversion rates and turnover efficiency (TOF) on the basis of the loading of Bi nanoparticles for Bi–1.0% rGO and Bi–1.0% $Ti_3C_2T_x$ are 0.552 mmol g_{Bi}^{-1} min^{-1} (6.92 NP^{-1} h^{-1}) and 0.642 mmol g_{Bi}^{-1} min^{-1} (8.05 NP^{-1} h^{-1}), respectively (Fig. 4b, Table S3†), which contradicts specific surface area and pore size analyses. It is reasonable to conclude that the enhanced catalytic ability of Bi–1.0% $Ti_3C_2T_x$ compared to Bi–1.0% rGO originates from the better hydrophilicity as confirmed by the contact angle measurements (Fig. 4c). This is because rGO possesses low-content hydrophilic surface functional groups (Fig. S13†).

The catalytic activities of the bulk sponge-confined Bi–1.0% $Ti_3C_2T_x$ and Bi–1.0% rGO are assessed by reducing 4-NA, 3-NA, and 2-NA. Evidently, the catalytic activity of sponge-confined Bi–1.0% $Ti_3C_2T_x$ is superior to that of sponge-confined Bi–1.0% rGO (Fig. S14†), which is due to the favourable wettability of Bi/$Ti_3C_2T_x$. Fig. 5 shows the durability test of the sponge-confined catalysts. The catalytic activities of sponge-confined Bi–1.0% $Ti_3C_2T_x$ are well sustained after being successively used ten times, while the sponge-confined Bi–1.0% rGO shows

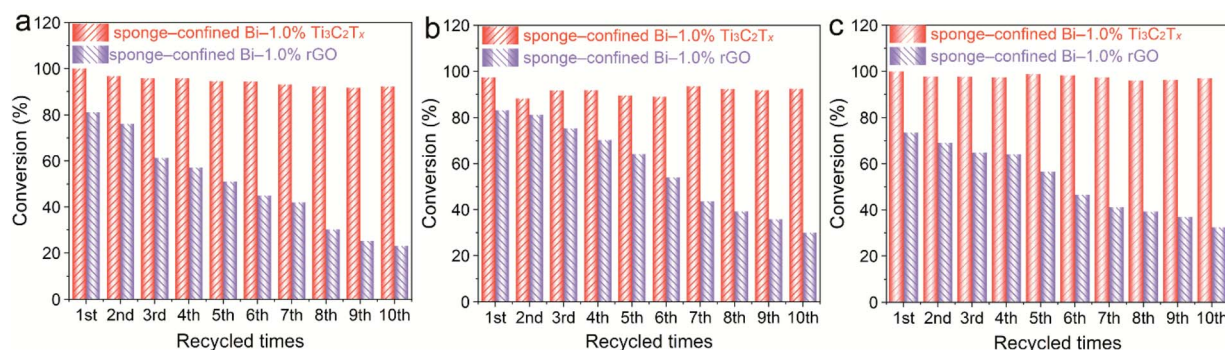**Fig. 5** Cycling tests for the conversion of (a) 4-NA, (b) 3-NA, and (c) 2-NA over sponge-confined Bi–1.0% $Ti_3C_2T_x$ and Bi–1.0% rGO.
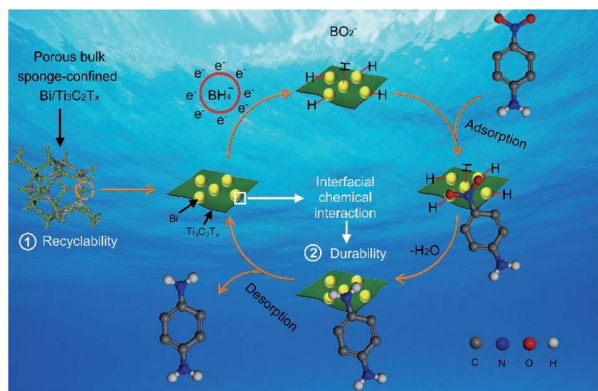
Fig. 6 The catalytic mechanism for the reduction of 4-NA over sponge-confined $Bi/Ti_3C_2T_x$.

considerably diminished catalytic activities. The durability of pristine Bi, Bi–1.0% $Ti_3C_2T_x$ and Bi–1.0% rGO is also examined. The conversion (%) of 4-NA over Bi–1.0% $Ti_3C_2T_x$ and Bi–1.0% rGO is nearly unchanged after five successive cycles of catalytic reactions (Fig. S15†), while it diminishes after each cycle for Bi, which suggests that $Ti_3C_2T_x$ and rGO can stabilize Bi. This is a result of the strongly interfacial chemical interaction between Bi and $Ti_3C_2T_x$ (rGO). With the combination of durability tests among Bi–1.0% $Ti_3C_2T_x$, Bi–1.0% rGO, sponge-confined Bi–1.0% $Ti_3C_2T_x$, and sponge-confined Bi–1.0% rGO, it can be concluded that the decrease in catalytic activities for sponge-confined Bi–1.0% rGO can be ascribed to the loss of Bi–1.0% rGO (Fig. S16†). The zeta potential of Bi–1.0% rGO (-14.31 mV) is less negative than that of Bi–1.0% $Ti_3C_2T_x$ (-20.71 mV) (Fig. 1c), which cannot afford strong electrostatic force to powerfully confine Bi–1.0% rGO on the APTES-modified sponge.

With the overall consideration of the analyses mentioned above, a credible mechanism for the hydrogenation of nitro-arenes over the sponge-confined $Bi/Ti_3C_2T_x$ is proposed[1,51] and schematically elucidated in Fig. 6. Firstly, BH_4^- reacts with water to generate BO_2^- and highly active H^-, followed by the swift adherence of the latter to $Bi/Ti_3C_2T_x$ to form Bi–H species. Secondly, nitroarenes are absorbed onto $Bi/Ti_3C_2T_x$ with their –NO_2 selectively getting close to the Bi–H species. Thirdly, the –NO_2 of nitroarenes reacts with Bi–H species *via* electron and mass transfer processes to form –NH_2. Finally, the reduced products are released from $Bi/Ti_3C_2T_x$ to liberate active sites for the next catalytic cycle. It should be noted that the interfacial chemical interaction-derived stabilization of Bi with $Ti_3C_2T_x$, the effective electrostatic confinement of the APTES-modified sponge towards $Bi/Ti_3C_2T_x$, and the high wettability of $Ti_3C_2T_x$ account for the improved durability, viable recyclability, and superior catalytic activity, respectively.

4 Conclusions

In summary, a sponge-confined $Bi/Ti_3C_2T_x$ catalyst is synthesized *via* the photodeposition of metallic Bi nanoparticles on $Ti_3C_2T_x$ and the strong electrostatic self-assembly between the negatively charged $Bi/Ti_3C_2T_x$ and APTES-modified sponge. The anchoring of metallic Bi nanoparticles on $Ti_3C_2T_x$ enables both the efficient utilization of active sites for strengthening catalytic activity and chemically stabilized catalytic durability. In comparison with rGO, $Ti_3C_2T_x$ with abundant hydrophilic surface groups as the support for attaching Bi nanoparticles favors both efficient aqueous catalytic reactions and electro-static interaction-derived recyclability. This study is expected to offer new strategy for designing cost-effective, stable, and easily recyclable integrated catalysts on the basis of economically porous bulk and 2D materials for catalytic reactions.

Author contributions

Changqiang Yu: methodology, conceptualization, investigation, formal analysis, and writing – original draft. Linfen Peng: resources, investigation, and visualization. Yisong Zhu: resources. Guanshun Xie: resources. Zhenjun Wu: resources. Xiuqiang Xie: project administration, supervision, and writing – review & editing. Nan Zhang: project administration, supervision, and writing – review & editing.

Conflicts of interest

There are no conflicts to declare.

Acknowledgements

Notes and references

1 Y. T. Yang, K. D. Jiang, J. Guo, J. Li, X. L. Peng, B. Hong, X. Q. Wang and H. L. Ge, *Chem. Eng. J.*, 2020, **381**, 122596.

2 P. Veerakumar, N. Dhenadhayalan, K. C. Lin and S. B. Liu, *J. Mater. Chem. A*, 2015, **3**, 23448–23457.

3 Q. Yan, X.-Y. Wang, J.-J. Feng, L.-P. Mei and A.-J. Wang, *J. Colloid Interface Sci.*, 2021, **582**, 701–710.

4 X. Q. Qiu, Q. W. Liu, M. X. Song and C. J. Huang, *J. Colloid Interface Sci.*, 2016, **477**, 131–137.

5 N. Zhang and Y. J. Xu, *Chem. Mater.*, 2013, **25**, 1979–1988.

6 R. Das, V. S. Sypu, H. K. Paumo, M. Bhaumik, V. Maharaj and A. Maity, *Appl. Catal., B*, 2019, **244**, 546–558.

7 Z. Hasan, D. W. Cho, C. M. Chon, K. Yoon and H. Song, *Chem. Eng. J.*, 2016, **298**, 183–190.

8 M. K. Dixit, D. Chery, C. Mahendar, C. Bucher and M. Dubey, *Inorg. Chem. Front.*, 2020, **7**, 991–1002.

9 J. Park, G. D. Saratale, S. K. Cho and S. Bae, *Sci. Total Environ.*, 2020, **705**, 134544.

19852 | *J. Mater. Chem. A*, 2021, **9**, 19847–19853

This journal is © The Royal Society of Chemistry 2021

10 J. Y. Yeh, B. M. Matsagar, S. S. Chen, H. L. Sung, D. C. W. Tsang, Y. P. Li and K. C. W. Wu, *J. Catal.*, 2020, **390**, 46–56.

11 K. Hareesh, R. P. Joshi, D. V. Sunitha, V. N. Bhoraskar and S. D. Dhole, *Appl. Surf. Sci.*, 2016, **389**, 1050–1055.

12 Y. Cui, K. B. Ma, Z. Chen, J. L. Yang, Z. G. Geng and J. Zeng, *J. Catal.*, 2020, **381**, 427–433.

13 N. Maity, A. Sahoo, R. Boddhula, S. Chatterjee, S. Patra and B. B. Panda, *Dalton Trans.*, 2020, **49**, 11019–11026.

14 H. Saikia, B. J. Borah, Y. Yamada and P. Bharali, *J. Colloid Interface Sci.*, 2017, **486**, 46–57.

15 T. A. Revathy, S. Dhanavel, T. Sivaranjani, V. Narayanan, T. Maiyalagan and A. Stephen, *Appl. Surf. Sci.*, 2018, **449**, 764–771.

16 E. Herrera, M. S. Aprea, J. S. Riva, O. F. Silva, P. G. Bercoff and A. Granados, *Appl. Surf. Sci.*, 2020, **529**, 147029.

17 B. Bhaduri and T. Polubesova, *Mater. Lett.*, 2020, **267**, 127546.

18 Y. Junejo, M. Safdar, M. A. Akhtar, M. Saravanan, H. Anwar, M. Babar, R. Bibi, M. T. Pervez, T. Hussain and M. E. Babar, *J. Inorg. Organomet. Polym. Mater.*, 2019, **29**, 111–120.

19 H. Chen, C. Liu, M. Wang, C. Zhang, N. Luo, Y. Wang, H. Abroshan, G. Li and F. Wang, *ACS Catal.*, 2017, **7**, 3632–3638.

20 W. Yue, M. F. Hao, B. Yu, R. Z. Ouyang and Y. Q. Miao, *Nanotechnology*, 2020, **31**, 145717.

21 J. K. Zhou, J. P. Gao, X. Y. Xu, W. Hong, Y. H. Song, R. N. Xue, H. L. Zhao, Y. Liu and H. X. Qiu, *J. Alloys Compd.*, 2017, **709**, 206–212.

22 C. Yu, Z. Tong, S. Li and Y. Yin, *Mater. Lett.*, 2019, **240**, 161–164.

23 C. Yu, M. Wen, Z. Tong, S. Li, Y. Yin, X. Liu, Y. Li, T. Liang, Z. Wu and D. D. Dionysiou, *Beilstein J. Nanotechnol.*, 2020, **11**, 407–416.

24 D. B. Jiang, X. Y. Liu, Y. S. Yuan, L. Feng, J. Y. Ji, J. S. Wang, D. Losic, H. C. Yao and Y. X. Zhang, *Chem. Eng. J.*, 2020, **383**, 123156.

25 J. Y. Liu, H. Xu, H. P. Li, Y. H. Song, J. J. Wu, Y. J. Gong, L. Xu, S. Q. Yuan, H. M. Li and P. M. Ajayan, *Appl. Catal., B*, 2019, **243**, 151–160.

26 X. D. Wang, J. He, J. Y. Li, G. Lu, F. Dong, T. Majima and M. S. Zhu, *Appl. Catal., B*, 2020, **277**, 119230.

27 Y. Zhang and S. J. Park, *Chem. Eng. J.*, 2019, **369**, 353–362.

28 B. Han, Y. L. Zhang, L. Zhu, Y. Li, Z. C. Ma, Y. Q. Liu, X. L. Zhang, X. W. Cao, Q. D. Chen, C. W. Qiu and H. B. Sun, *Adv. Mater.*, 2019, **31**, 1806386.

29 Y. Fu, T. Mei, G. Wang, A. K. Guo, G. C. Dai, S. Wang, J. Y. Wang, J. H. Li and X. B. Wang, *Appl. Therm. Eng.*, 2017, **114**, 961–968.

30 Y. X. Duan, K. H. Liu, Q. Zhang, J. M. Yan and Q. Jiang, *Small Methods*, 2020, **4**, 1900846.

31 B. K. Barman, B. Sarkar, R. Nandan and K. K. Nanda, *New J. Chem.*, 2021, **45**, 1556–1564.

32 X. Q. Xie, N. Zhang, Z. R. Tang, M. Anpo and Y. J. Xu, *Appl. Catal., B*, 2018, **237**, 43–49.

33 M. Naguib, M. Kurtoglu, V. Presser, J. Lu, J. J. Niu, M. Heon, L. Hultman, Y. Gogotsi and M. W. Barsoum, *Adv. Mater.*, 2011, **23**, 4248–4253.

34 V. Kamysbayev, A. S. Filatov, H. C. Hu, X. Rui, F. Lagunas, D. Wang, R. F. Klie and D. V. Talapin, *Science*, 2020, **369**, 979–983.

35 X. Q. Xie and N. Zhang, *Adv. Funct. Mater.*, 2020, **30**, 2002528.

36 Y. Liu, Y.-H. Li, X. Li, Q. Zhang, H. Yu, X. Peng and F. Peng, *ACS Nano*, 2020, **14**, 14181–14189.

37 S. Min, Y. Xue, F. Wang, Z. Zhang and H. Zhu, *Chem. Commun.*, 2019, **55**, 10631–10634.

38 L. Liu, Q. Zhao, R. Liu and L. Zhu, *Appl. Catal., B*, 2019, **252**, 198–204.

39 F. Song, G. H. Li, Y. S. Zhu, Z. J. Wu, X. Q. Xie and N. Zhang, *J. Mater. Chem. A*, 2020, **8**, 18538–18559.

40 J. X. Low, B. Z. Dai, T. Tong, C. J. Jiang and J. G. Yu, *Adv. Mater.*, 2019, **31**, 1802981.

41 E. Jeong, J. Byun, B. Bayarkhuu and S. W. Hong, *Appl. Catal., B*, 2021, **282**, 119587.

42 C. L. Li, M. C. Wu and R. Liu, *Appl. Catal., B*, 2019, **244**, 150–158.

43 J. Yang, X. Wang, B. Li, L. Ma, L. Shi, Y. Xiong and H. Xu, *Adv. Funct. Mater.*, 2017, **27**, 1606497.

44 X. Q. Xie, Z. J. Wu and N. Zhang, *Chin. Chem. Lett.*, 2020, **31**, 1014–1017.

45 J. Li, X. T. Yuan, C. Lin, Y. Q. Yang, L. Xu, X. Du, J. L. Xie, J. H. Lin and J. L. Sun, *Adv. Energy Mater.*, 2017, **7**, 1602725.

46 Q. Hao, R. T. Wang, H. J. Lu, C. A. Xie, W. H. Ao, D. M. Chen, C. Ma, W. Q. Yao and Y. F. Zhu, *Appl. Catal., B*, 2017, **219**, 63–72.

47 X. Q. Xie, C. Chen, N. Zhang, Z. R. Tang, J. J. Jiang and Y. J. Xu, *Nat. Sustain.*, 2019, **2**, 856–862.

48 T. T. Hou, Q. Q. Luo, Q. Li, H. L. Zu, P. X. Cui, S. W. Chen, Y. Lin, J. J. Chen, X. S. Zheng, W. K. Zhu, S. Q. Liang, J. L. Yang and L. B. Wang, *Nat. Commun.*, 2020, **11**, 4251.

49 T. Cai, L. L. Wang, Y. T. Liu, S. Q. Zhang, W. Y. Dong, H. Chen, X. Y. Yi, J. L. Yuan, X. N. Xia, C. B. Liu and S. L. Luo, *Appl. Catal., B*, 2018, **239**, 545–554.

50 K. Peng, L. J. Fu, H. M. Yang, J. Ouyang and A. D. Tang, *Nano Res.*, 2017, **10**, 570–583.

51 X. Y. Yang, Y. Li, P. Zhang, R. M. Zhou, H. L. Peng, D. Liu and J. Z. Gui, *ACS Appl. Mater. Interfaces*, 2018, **10**, 23154–23162.

This journal is © The Royal Society of Chemistry 2021

J. Mater. Chem. A, 2021, **9**, 19847–19853 | **19853**